Journal of Materials Chemistry B

ROYAL SOCIETY OF CHEMISTRY

PAPER

View Article Online
View Journal | View Issue

Open Access Article. Published on 05 December 2025. Downloaded on 3/6/2026 5:47:09 PM.
This article is licensed under a Creative Commons Attribution 3.0 Unported Licence.

Check for updates

Cite this: J. Mater. Chem. B, 2026, 14, 342

Elucidation of how metal layer deposition conditions impact the optical responses of microgel-based etalon devices to stimuli

Haley Hunter and Michael J. Serpe *

Received 14th July 2025,
Accepted 28th November 2025

DOI: 10.1039/d5tb01640a

rsc.li/materials-b

Poly(*N*-isopropylacrylamide) (pNIPAm) microgel-based etalons exhibit visual color, and can be fabricated by sandwiching a monolithic microgel layer between two thin metal layers (typically Au). The color of the devices is a direct result of the device structure, and can be dynamically tuned by varying the thickness of the microgel layer in response to external stimuli. For many applications, the robustness of the etalon's structure, the spatial uniformity of the color, and the color change kinetics are of utmost importance. In this investigation, we determined how the composition of the layers that make up the etalon impacts their performance. Specifically, the results indicated that stable etalons can be constructed by simply depositing a layer of Au on top of the microgel layer, as opposed to using a Cr adhesion layer on top of the microgels prior to Au overlayer deposition. We show that thin Au overlayers without a Cr adhesion layer produces Au films that are discontinuous in nature, which in turn directly influences the kinetics of the etalon response. We also confirm that this response pattern holds true for etalon responses to various salt solutions, presenting potential for the future application to alternative analytes of interest.

Introduction

In an increasingly complex world landscape, new health and environmental monitoring and sensing technologies are essential to ensure longevity in these symbiotic areas. For example, those residing in urban centers have relatively ready access to testing/diagnostic resources, compared to those in rural/remote settings. Current cutting-edge monitoring and sensing technologies are often expensive, time consuming and use tools that must be operated by trained professionals in a lab environment; this is not always feasible for those in rural/remote settings. Hence, those that reside in remote or resource-limited areas are disadvantaged, as they are not as equipped to make informed decisions.[1–3] Point-of-need sensors are a group of important technologies that can help fill this void. Ideally, point-of-need sensors are devices that can be deployed outside of a laboratory setting, by untrained users, and provide test results where they are needed quickly, with performances comparable to what can be achieved in the lab. This field of research has been rapidly growing over the past decade, with significant advances made using lateral flow assays,[2,4–6] plasmonic sensors[7–9] and portable smartphone-based colorimetric sensors.[10–12] While many advances have been made in recent years, new materials are constantly being investigated to help advance the field even further.

Optical sensors are of particular interest as their results can be recorded by the naked eye or *via* photographs from a camera. Many of the technologies used for fabricating optical sensors are photonic materials, which use light to detect and quantify analytes.[13] Photonic crystals are made up of at least two materials of different refractive indexes arranged periodically in one-, two- or three-dimensions. Photonic crystals can exhibit visible color, and have many advantages over conventional colorimetric sensing technologies, *e.g.*, there's no photobleaching issues, and they are relatively simple to modify for quantifying multiple analytes simultaneously.[14,15]

The Serpe Group has developed a photonic material-based sensing device that utilizes a hydrogel particle (microgel) layer sandwiched between two thin Au layers.[16–18] This device exhibits visual color, and multipeak reflectance spectra, due to the structure of the device, *i.e.*, light enters the microgel-based cavity and undergoes constructive and destructive interference. The color of the device, and the position of the reflectance peaks, depends on the thickness of the microgel layer, which sets the distance between the two Au layers. Importantly, the microgel layer responds to stimuli by swelling or shrinking, thus changing the distance between the two Au layers, the color of the device, and the position of the reflectance peaks.

Department of Chemistry, University of Alberta, Edmonton, AB, T6G 2G2, Canada. E-mail: serpe@ualberta.ca

 This journal is © The Royal Society of Chemistry 2026

Open Access Article. Published on 05 December 2025. Downloaded on 3/6/2026 5:47:09 PM.
This article is licensed under a Creative Commons Attribution 3.0 Unported Licence.

The position of the reflectance peaks can be calculated using eqn (1):

$$\lambda_m = 2nd\cos\theta \quad (1)$$

where λ is the maximum wavelength of the peak(s), m is the peak order, n is the refractive index of the cavity material, d is the spacing between the Au layers (dictated between the microgel layers), and θ is the angle of incidence.[17,19] As λ is proportional to d, λ shifts with changing microgel layer thickness, so long as all other variables remain constant. Note that the microgel layer n does vary with microgel layer thickness, although in many cases the changes are small relative to d.

The microgels used here are primarily composed of poly(*N*-isopropylacrylamide) (pNIPAm), which is a well-known thermo-responsive polymer that exhibits a lower critical solution temperature (LCST) at ~32 °C, leading to a reversible demixing (collapse) of the polymer chains above this temperature.[20–23] Hence, crosslinked pNIPAm-based microgels decrease in diameter substantially at temperatures above the LCST, which is referred to as the volume phase transition temperature (VPTT). In our devices, this change in microgel size with temperature can be harnessed to change the optical properties of the microgel-based etalons (according to the equation above). Inclusion of a copolymer in the pNIPAm microgels expands the potential applications of the etalons as they can respond to other stimuli in addition to temperature. A common comonomer that is used is acrylic acid (AAc), which imparts pH responsivity to the microgels.[22] It has been shown that these microgels are also affected by the presence of ions in solution, changing the solvation state of the microgels and therefore affecting the color of the etalon device.[24–27] Previously, our group has worked on variations of these microgel-based etalons that respond to different analytes. For example, we have generated etalons that respond to methanol,[28] free phosphate,[29] volatile organic compound vapours,[30] progesterone[31] and glucose.[32]

This study aims to expand our understanding of the response characteristics of our etalon-based sensing system, and while this is of utmost importance to our group, it has implications in the broader sensor community. For example, Jung *et al.* published work on an etalon-based humidity sensor and anti-counterfeiting display that involves a mirror-hydrogel-metal nanoparticle structure.[33] Wang *et al.* have also developed an etalon-based sensor with a pNIPAm composite as the cavity material for sensing temperature and humidity.[34] Dong *et al.* developed optical etalon-based sensors using Au film-hydrogel-Au film structures for humidity sensing and Palinski *et al.* published similar Au–polymer–Au structures for organic vapour sensing.[35,36] Etalons are not the only photonic device structure that is of interest for this work, distributed Bragg reflector-based sensors are also being developed from similar material components.[37]

Over recent years our group has introduced a series of optimizations and changes to our etalon system which left us with a need to investigate the structures and responses of the new system. This fundamental study into the dependence of device response on structure was driven by a need for knowledge and understanding of the system before further exploration into sensor applications.

Materials and methods

Materials

N-Isopropylacrylamide (NIPAm) was purchased from TCI America (Portland, Oregon) and purified by recrystallization with hexane prior to use. *N′N*-methylenebisacrylamide (BIS), acrylic acid (AAc), ammonium persulfate (APS), ammonium chloride, tetraethylammonium chloride and tetramethylammonium chloride were purchased from MilliporeSigma (Oakville, Ontario). Ethanol (100%), sodium chloride and sodium hydroxide were purchased from Fisher Scientific (Saint Laurent, Quebec). Hydrochloric acid was purchased from Caledon Laboratory Chemicals (Georgetown, Ontario). Milli-Q deionized water (18.2 MΩ cm) from a Millipore Milli-Q-Plus system (Billerica, Massachusetts) was used for all experiments. Glass substrates (10 × 10 mm cover glass #1.5) were purchased from Ted Pella Inc (Redding, California). Microfluidic chips and corresponding tubing/connectors were acquired from Microfluidic Chip Shop (Jena, Germany). A Raspberry Pi Camera Module v2 (Wales, UK) in a custom 3D-printed container was used for all imaging. Graphics were created with biorender.com.

Microgel synthesis

Poly(*N*-isopropylacrylamide-*co*-acrylic acid) (pNIPAm-*co*-AAc) microgels were synthesized by free radical precipitation polymerization, adapted from previously described methods.[16,38] A total monomer concentration of 140 mM was used. NIPAm (29.8 mmol) and BIS (1.76 mmol) were dissolved in 250 mL of deionized water followed by filtration through a 0.2 μm filter. The solution was purged with N_2(g) and temperature ramped from 20 to 70 °C over 1.5 h. AAc (3.58 mmol) diluted in 1 mL of deionized water was then added to the monomer solution, followed by APS (0.5 mmol) to initiate polymerization. The reaction was allowed to proceed for 3 h at 70 °C followed by cooling overnight. The microgel solution was filtered through Whatman #1 filter paper to remove any aggregates and washed by centrifugation and resuspension 6 times to remove any unreacted monomer. The resulting microgel solution was centrifuged to remove excess water and obtain the ideal viscosity for etalon fabrication, or an approximate microgel concentration of 55 mg mL^{-1}. The resulting microgels synthesized with this method have a hydrated diameter of approximately 800 nm.

Etalon fabrication

Our group has previously reported a "paint-on" protocol for fabrication of microgel-based etalons, and that method was adapted for this work.[18] 10 × 10 × 0.17 mm glass coverslips were precleaned by sonication in ethanol and deionized water, followed by drying under a stream of N_2 gas. Au-coated glass substrates were fabricated by sputter coating 2 nm of Cr

Open Access Article. Published on 05 December 2025. Downloaded on 3/6/2026 5:47:09 PM.
This article is licensed under a Creative Commons Attribution 3.0 Unported Licence.

(0.38 nm s^{-1}) followed by 15 nm Au (0.24 nm s^{-1}) using a planar magnetron sputter system. Coated glass substrates were then exposed to ~100 μL of concentrated microgel solution that was spread over the surface using a "doctor blading" technique. The doctor blading method used involves placing a glass substrate in a custom metal slide holder, pipetting a strip of concentrated microgels (~100 μL) along one edge of the holder and then "doctor blading" the microgel solution over the substrate surface using a clean 25 × 75 × 1 mm glass slide held at a ~45° angle.[39] Substrates were then placed on a hot plate at 35 °C to dry for ~2 h followed by rinsing under stream of deionized water to remove unbound microgels and soaked in deionized water overnight at 30 °C. Finally, substrates were rinsed again under a stream of deionized water and dried under N_2 gas. The etalon overlayer was then deposited using the same sputter coating system with same deposition rates, the thickness of Cr and/or Au varied for different samples.

Scanning electron microscopy

The structure of the metal films generated by different Cr/Au compositions was characterized by a Hitachi S-4800 FESEM high resolution scanning electron microscope (SEM). Imaging was done using 5.0 kV accelerating voltage, 4 mm working distance and 70 k or 100 k magnification.

Au overlayer stability

To investigate the metal overlayer stability at different conditions, and how it's impacted by the presence of a Cr adhesion layer, samples with 2 nm Cr/5 nm Au and 0 nm Cr/5 nm Au were compared. Samples were placed in microfluidic chips (custom chips from Microfluidic Chip Shop) and subjected to 3 types of testing. First, we assessed stability upon water flushing. To do this, etalons were stored in deionized water, and every ~24 h fresh deionized water was flowed over the etalon at a rate of 0.25 mL min^{-1} for 60 s, equilibrated for 30 min and then an image of the etalon was captured. This was repeated for seven days. The next round of testing used etalons stored in deionized water, and every ~24 h a 0.25 M NaCl solution was flowed over the etalon at a rate of 0.25 mL min^{-1} for 60 s and equilibrated for 30 min followed by image capture. These etalons were then flushed with deionized water and stored until the next day, and the cycle was repeated for seven days. Lastly the same process (with the same flow rate and run times) was completed except etalons were stored in pH 4 deionized water and flushed with pH 8 deionized water daily for seven days.

Reflectance spectroscopy

All reflectance spectra were collected using an Ocean Optics (Orlando, Florida) USB2000+ Fibre Optic Spectrometer, NIR-vis optical fibre, and SpectraSuite Software. World Precision Instruments (Sarasota, Florida) Aladdin single-syringe infusion pumps were used to deliver solutions into the microfluidic chips containing the etalons. For hydration experiments the sample was loaded in its dry state and deionized water was introduced at a rate of 0.25 mL min^{-1} for 2 min, then sample monitoring was continued for an additional 58 min, capturing a spectrum every 5 s for the hour. For salt response experiments the samples underwent 4 salt-water cycles, followed by equilibration in deionized water overnight prior to testing. Salt solutions were introduced under the same conditions as hydration experiments.

Results and discussion

Structure and stability of the various metal overlayers

Etalons are fabricated by depositing a thin Cr/Au film onto a clean glass substrate. A viscous solution of microgels are then spread over the surface and left to dry above their VPTT. This enables the microgel to collapse and pack tightly together onto the surface, the soft nature of the microgels also enables this tight packing behaviour. Both the microgel–microgel interations as well as the microgel–surface interactions play a role in the assembly of the film.[16–18,28]

Initially, we investigated how the etalon overlayer composition impacted its response. Specifically, our group has traditionally made etalons using Cr and Au in both the base layer and overlayer of the etalon (Scheme 1).[16–18,40] It is known that Cr is required in the base layer to adehere the Au layer to the glass, however it may not be needed for adhesion of the Au layer to the microgels in the overlayer.[41]

To explore this, etalons were made with the following overlayer compositions – 0 nm Cr/5 nm Au, 0 nm Cr/15 nm Au, 2 nm Cr/5 nm Au, 2 nm Cr/15 nm Au, 5 nm Cr/5 nm Au, and 5 nm Cr/15 nm Au. These thicknesses are based on the rate of metal deposition determined through calibrations of the sputter coating system. The actual thicknesses of the films may slightly differ from these nominal values, however the observed trends and conclusions made throughout this study are still valid. The structure of these different films was evaluated using images obtained *via* SEM (Fig. 1). From the images, we observed that the samples containing 2 or 5 nm of Cr in the overlayer had a more continuous film structure than those without Cr. Based on previous studies of Au film growth on different substrates, we propose this phenomenon is a result of Au deposited on Cr having a different film growth mechanism than Au deposited on the microgel layer.[42–44] From the literature we know that when Au films are deposited on glass substrates the Au nuclei undergo dewetting type growth, and as these nuclei coalesce they leave voids and structural discontinuities in the film structure. However, when Au is

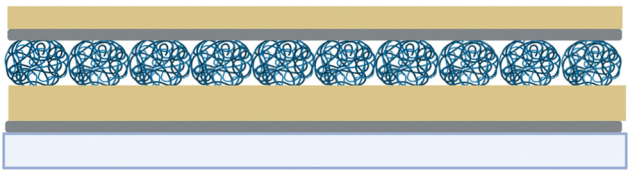

Scheme 1 Schematic of the general etalon structure from bottom to top: glass coverslip, Cr/Au metal base layer, microgel, (Cr)/Au metal overlayer. Created with BioRender.com.

Open Access Article. Published on 05 December 2025. Downloaded on 3/6/2026 5:47:09 PM.
This article is licensed under a Creative Commons Attribution 3.0 Unported Licence.

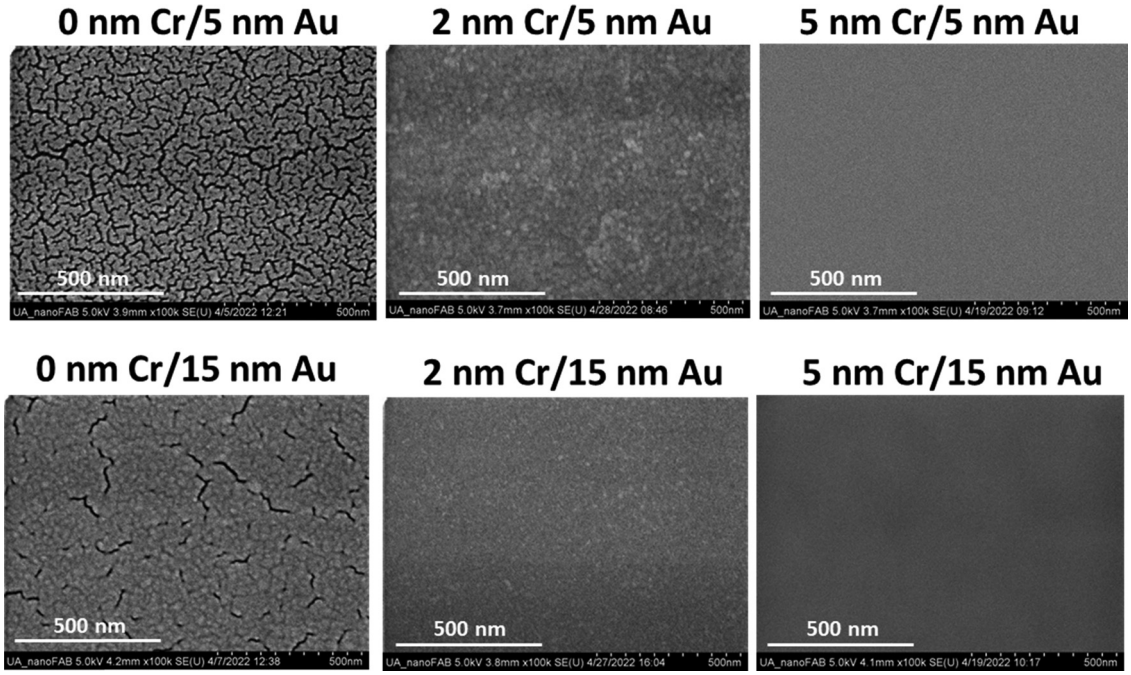

Fig. 1 Scanning electron microscopy images of various Cr/Au overlayer compositions deposited onto microgel films to generate the etalons.

deposited onto a layer of Cr the Au nuclei undergo wetting type growth, meaning the nuclei grow along the surface rather than away from the surface, generating a more continuous final film structure.[45–49] Based on this, it appears that the Au being deposited onto the microgel layer follows the same growth mechanisms, apparent dewetting without Cr and apparent wetting with Cr. It is also observed that increasing total film thickness leads to a more continuous structure, this is hypothesized to be due to the nuclei coalescing with increased material deposition.[45–49]

Next, we investigated whether the underlying irregularities of the microgel films led to cracks/discontinuities in the deposited Au overlayers. To accomplish this, we deposited the same film combinations as above directly onto clean/bare glass substrates, *i.e.*, no microgels or base Cr/Au layers. As can be seen in Fig. 2, similar overall film structures were observed when the metal films were deposited directly on glass, compared to the metal layers deposited on the microgel layer (see Fig. 1). Major discontinuity and visible cracks/openings in the film structures are only present in the Cr free metal layers for both sets of samples. We note that the 15 nm Au samples exhibit some inconsistencies in their structures for the different substrates; the film on microgels has larger "cracks" compared to the film on glass. This could be due to influences from the surface of the microgels themselves. However the impact of Cr and film thickness on structure appears to be consistent for both substrates. As the metal films appear to develop with overall similar structures whether deposited directly onto the glass or onto the microgel layer we concluded that in this case the different structures are predominanlty a result of the different growth mechanisms rather than the different substrate surfaces. In other words, the heterogeneity that comes from the microgel layer is not presumed to be the main cause of the discontinuous film structures, but rather the lack of Cr and thickness of the film are more important.

Since we were able to make the Au overlayers on the microgel layer without Cr, we went on to investigate how robust the overlayers were upon use. To do this, etalons were inserted into microfluidic chips, and solution flowed over them while the structure (as observed as color) of the etalons was monitored. If the overlayer deteriorates we would expect to see sections of the etalon with no color, which would mean that the etalon structure was degrading. First, we explored if the etalon structure withstood hydration and gentle agitation from solution flow. For seven days the etalons were kept hydrated inside the microfluidic chips. Once a day we pumped fresh water through the microfluidic chips and then an image of the etalon was captured to monitor the film integrity over time (Fig. 3a–d). Next, we explored if triggering the microgels to change solvation state (resulting in an etalon color change) causes the overlayers to destabilize. To do this, etalons were exposed to solutions of varying ionic strength and pH, and the data can be seen Fig. 3e–h and Fig. 3i–l, respectively. Although there are slight color fluctuations over time, the films appear to stay intact throughout all challenges, therefore we concluded that the Cr is not necessary for the etalon to reliably function in the microfluidic chips.

This stability of the films was also explored on a microscopic level using SEM analysis. In Fig. 4 the overlayer structure of a 0 nm Cr/5 nm Au etalon was imaged using SEM before (a) and after (b) etalon hydration. From these images we can see that the behavior observed in Fig. 3 was supported, *i.e.*, that the structure of the films appears to remain unchanged after device modulation. These combined observations left us confident

Open Access Article. Published on 05 December 2025. Downloaded on 3/6/2026 5:47:09 PM.
This article is licensed under a Creative Commons Attribution 3.0 Unported Licence.

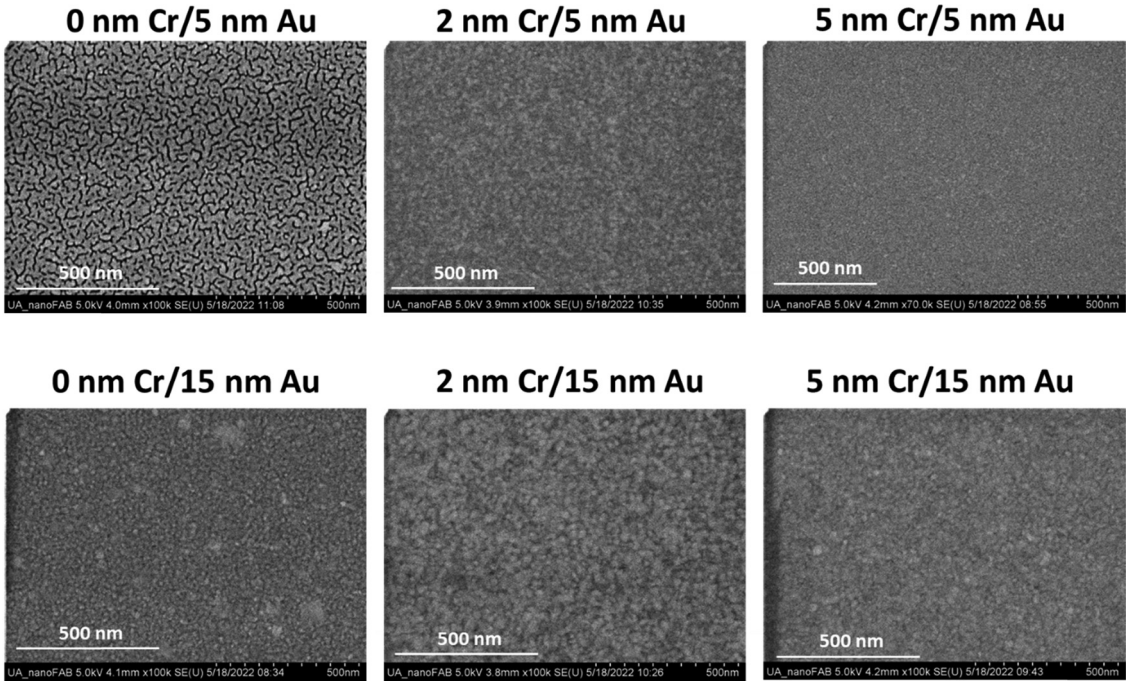

Fig. 2 Scanning electron microscopy images of the indicated metals deposited onto bare glass substrates.

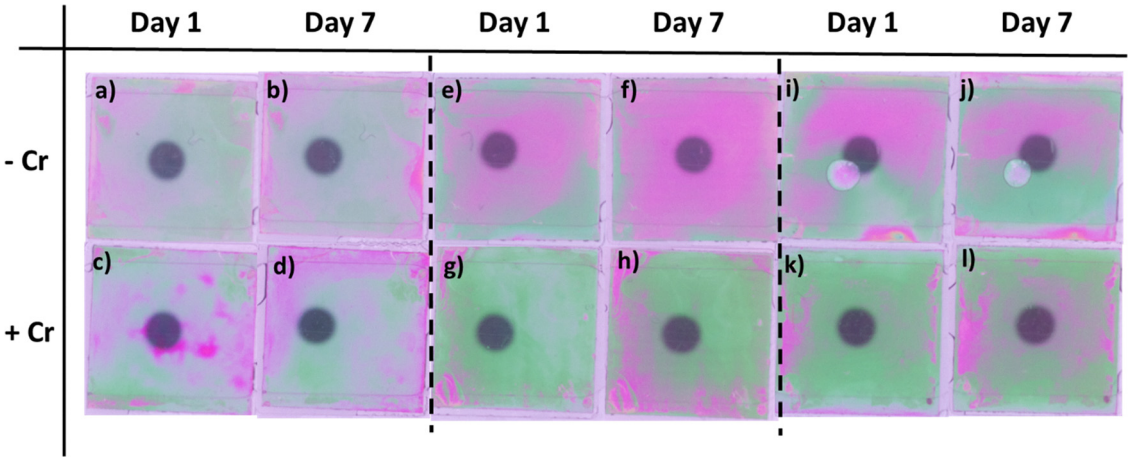

Fig. 3 Images (taken using a Raspberry Pi camera) of etalons before and after stability testing with water flow (a)–(d), salt-water cycling (e)–(h), and pH cycling (i)–(l). Center black spot due to the reflection of the camera.

that the Cr adhesion layer is not requirement for stable etalon overlayers.

Hydration and salt response time as a function of overlayer composition

A major benefit of point-of-need sensing over traditional laboratory-based methods is that results can be obtained quickly. After characterizing the different etalon overlayers and observing that those with only thin Au layers (no Cr) exhibited discontinuous structure *i.e.*, cracks in the film, we hypothesized that these etalons would respond to changes in their environment faster than the others. This prediction is founded in the knowledge that for the etalon to respond to an analyte it must either diffuse through the Au overlayer or through the sides of the device into the microgel-based cavity. For the etalon to respond to the analyte, water must also be able to diffuse into/out of the microgels (Scheme 2a) and the device (Scheme 2b). With this understanding we hypothesize that the cracks in the overlayer should allow for easier analyte/water exchange and therefore faster overall device response. With the following set of experiments, we set out to determine if having a discontinuous (cracked) metal overlayer would allow the etalon to respond to changes in its environment more rapidly than the traditional etalon made with a continuous metal overlayer.

To achieve this, we determined the kinetics of hydration for the different etalons to assess how easily water molecules enter

 This journal is © The Royal Society of Chemistry 2026

Open Access Article. Published on 05 December 2025. Downloaded on 3/6/2026 5:47:09 PM.
This article is licensed under a Creative Commons Attribution 3.0 Unported Licence.

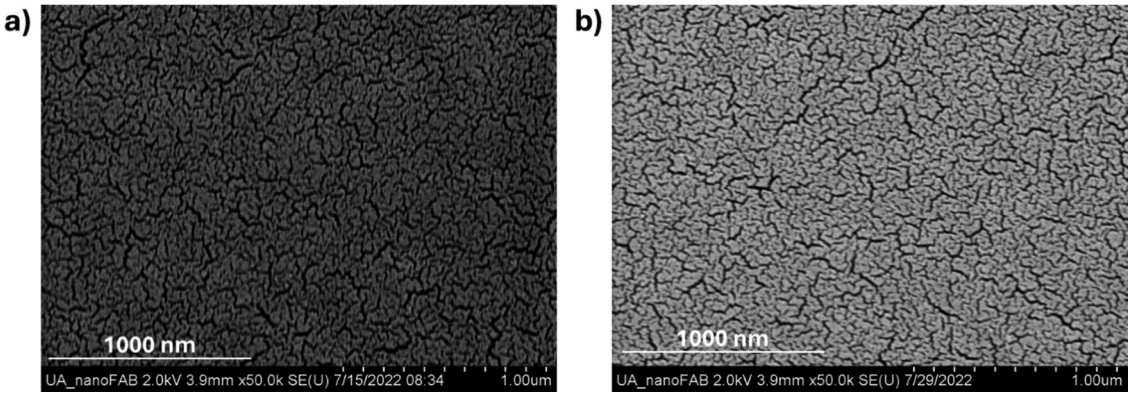

Fig. 4 Scanning electron microscopy image of a 0 nm Cr/5 nm Au sputter coated etalon before (a) and after (b) the etalon has undergone hydration in deionized water. 1000 nm scale bars.

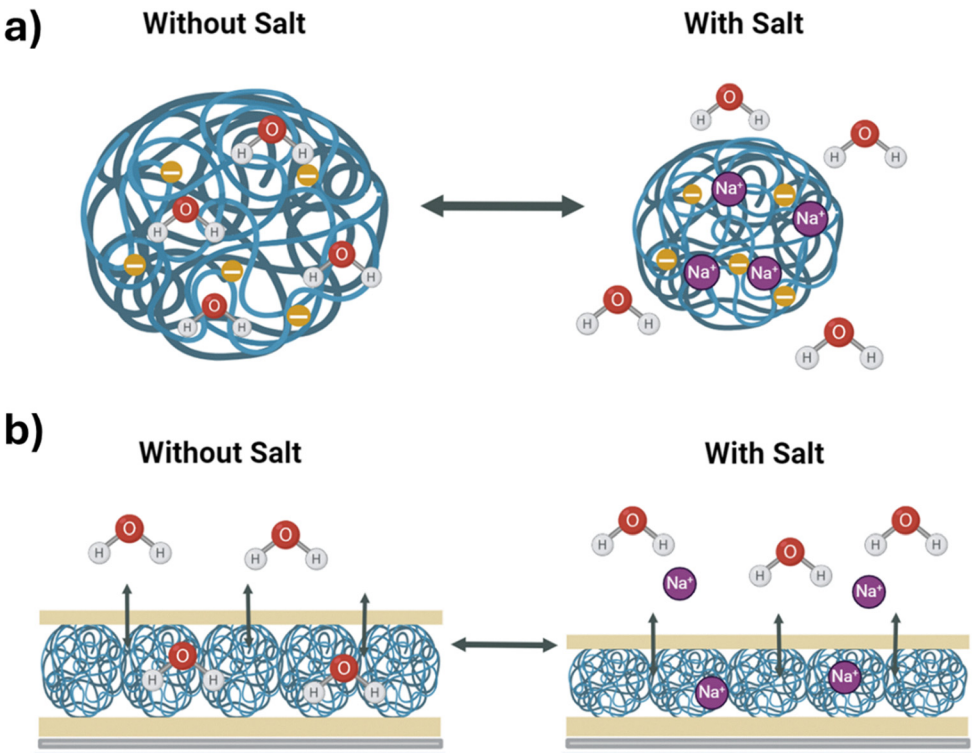

Scheme 2 Methods of microgel and etalon responses, (a) the microgel actuation upon response to solution changes and (b) showing analyte diffusion into the etalon cavity. Created with BioRender.com.

the microgels in the cavity; we also determined the kinetics of their response to the introduction of salt to assess how easily analyte/water exchange occurs. For the remaining analyses the data was collected from monitoring the reflectance spectra of the etalons using an optical probe and UV-visible spectrophotometer. The wavelength shifts in the location of the peaks and/or valleys of the reflectance spectra are measured to quantify the response of the etalons (an example spectra is shown in Fig. 5).

We started with investigating how quickly each etalon design was able to transition from a dry to hydrated state. Dry etalons were secured into microfluidic chips followed by deionized water injection into the chip, and the etalons were left to equilibrate. As can be seen in Fig. 6 the 0 nm Cr/5 nm Au sample reached a hydrated state nearly immediately. The 0 nm Cr/15 nm Au sample was the next fastest to respond, but it is still 20 times slower than the 5 nm Au sample. The remaining etalons took longer to hydrate, from around 300 s to around 2000 s. This helps corroborate our hypothesis that the discontinuous films improve response time.

After observing the drastic difference in etalon hydration, we further investigated the response of the etalons to changes in

Open Access Article. Published on 05 December 2025. Downloaded on 3/6/2026 5:47:09 PM.
This article is licensed under a Creative Commons Attribution 3.0 Unported Licence.

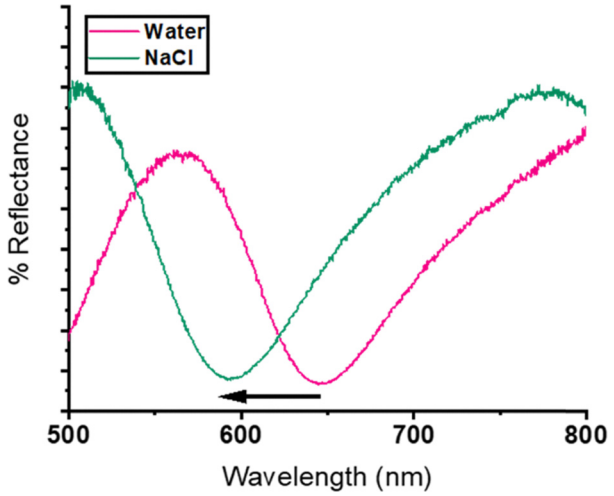

Fig. 5 Example of a reflectance spectra of an etalon using an optical probe, both in deionized water (pink) and in an NaCl salt solution (green).

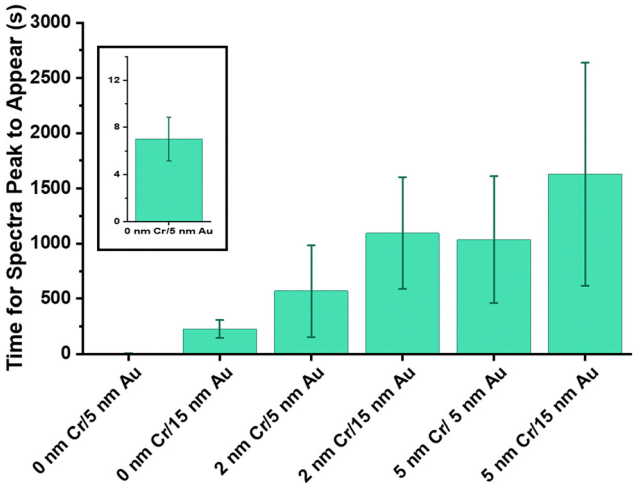

Fig. 6 Plot of the time (s) taken for etalons with different metal overlaters to hydrate (time for a spectral peak to appear) from the starting dry state. Inset included to show the difference in scale for the response of the 0 nm Cr/5 nm Au samples. Two regions on each etalon were monitored, five etalons of each type were measured therefore the average and standard deviation are plotted, with n = 10.

salt concentration. Etalons that had been previously hydrated were used for these experiments. We have observed that the first salt response of unused etalons is significantly different than its subsequent responses, therefore before salt response experiments were executed, all etalons were pre-treated by exposure to salt and water over four cycles followed by equilibration in deionized water. Fig. 7a shows the average peak shifts over time for the various etalons with different Cr/Au overlayer combinations. We observed that the 0 nm Cr/5 nm Au etalons exhibit a different kinetic curve than the other etalons. This is thought to be due to its rapid response, likely from a rush of ions into the microgel before reaching an equilibrium state (Fig. 7c).[24] Whereas the other etalons gradually reach equilibrium without the initial "over shift". This experiment was also completed using a set of etalons with increasing amounts of Au in the overlayer (never any Cr), those results can be seen in Fig. 7b. Samples with 5 (similar to 0 nm Cr/5 nm Au) and 10 nm of Au both exhibit a curve with an initial "over shift" before reaching an equilibrium state whereas samples with 15 nm or more of Au do not. This "overshift" of the etalons occurs only when the overlayers are relatively thin and discontinuous. We hypothesize that the limited barrier that these overlayers provide to solution exchange allows for near-immediate entry of the salt solution into the etalon cavity and subsequently into the microgels to cause a collapse and color shift. The etalon then reaches an equilibrium state. The structure of the overlayer is the only difference between the etalons, therefore we hypothesize that this is the cause for this observation.

After observing the differing salt response kinetics of the different etalons we related the responses back to the film structures. Using the SEM images, we approximated the void area of the etalon overlayer, or the area that is occupied by the cracks in the Au (Fig. 8a). To approximate the void area, SEM images were analyzed in ImageJ. Briefly, the images were converted to binary masks and the percent area of the image that was black could be quantified. We then extrapolated this calculated void space of the imaged area to the total area of the etalon surface. In Fig. 8b we can see the relationship between the decrease in response rate with increasing Au thickness and void area. This increasing response rate with Au thickness is likely due to the thickness of the overlayer reaching a threshold (or a certain void area) where the ion influx into the cavity is slowed by the more continuous overlayer, in this case the threshold is thought to be ~15 nm Au based on the data.

Etalon response to different cations

After previous experiments revealed that etalon hydration and salt response are affected by varying overlayer compositions we wanted to determine if the observed rapid response of etalons with certain overlayer structures relied on the cation itself. The microgels used throughout all of this study contain acrylic acid, which are negatively charged at neutral pH. The response of these microgels to salt is considered to be due to the positively charged cations relieving the charge repulsion within the microgels (Scheme 2). We wanted to identify if the properties of the cation in solution plays a role in the response of etalons with different overlayer structures (*i.e.* cracked/discontinuous vs continuous film). Therefore, we conducted a series of experiments investigating the response time of etalons to different cations and solution concentrations. We used four different chloride salts for this experiment: sodium, ammonium, tetramethylammonium, and tetraethylammonium. Eight different concentrations of each salt were studied, from 10 mM to 1280 mM; concentrations higher than this led to peak shifts too rapid to accurately quantify with our current methods. Etalons with 10 nm Au or 20 nm Au were used to explore the different Au overlayer thickness effects. We chose 10 nm and 20 nm of Au for this study to represent a discontinuous

 This journal is © The Royal Society of Chemistry 2026

Open Access Article. Published on 05 December 2025. Downloaded on 3/6/2026 5:47:09 PM.
This article is licensed under a Creative Commons Attribution 3.0 Unported Licence.

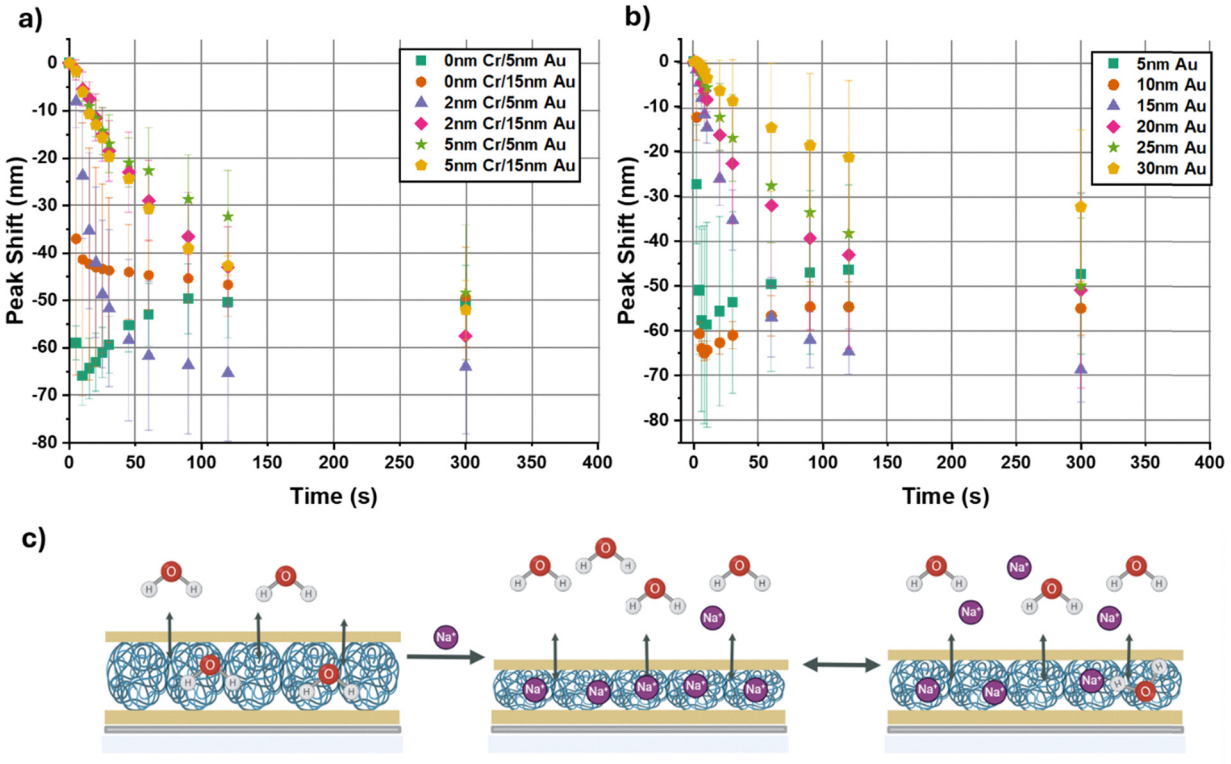

Fig. 7 Average peak shift kinetics of sputter coated etalons of various overlayer compositions over 5 minutes of NaCl exposure (a) and etalons of Au only overlayers (b). Average and standard deviation of each etalon type from n = 3. (c) Schematic depicting the "overshift," or influx on Na^+ ions, of the etalons containing discontinuous overlayers (0 nm Cr/5 nm Au, 5 nm Au, and 10 nm Au). Created with BioRender.com.

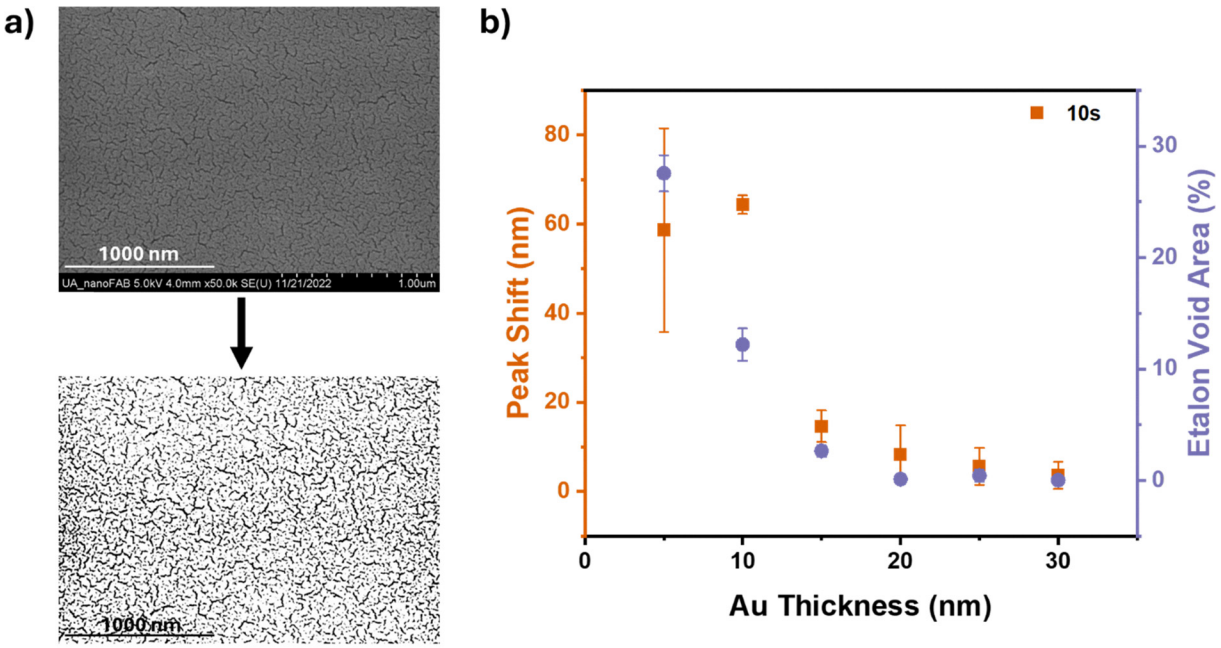

Fig. 8 (a) An example of the use of SEM images to approximate the void area of the cracks in the overlayer and (b) the comparison of the average peak shifts in the first 10 s to etalon void area as a function of Au thickness of the etalon overlayer. Average and standard deviations of both the peak shifts and void area percentages are from n = 3 etalons.

overlayer (etalon that exhibits an "over shift") and a continuous overlayer, respectively.

Results compiled from this study can be seen in Fig. 9. The data is represented with two categories of plots: the initial peak

Open Access Article. Published on 05 December 2025. Downloaded on 3/6/2026 5:47:09 PM.
This article is licensed under a Creative Commons Attribution 3.0 Unported Licence.

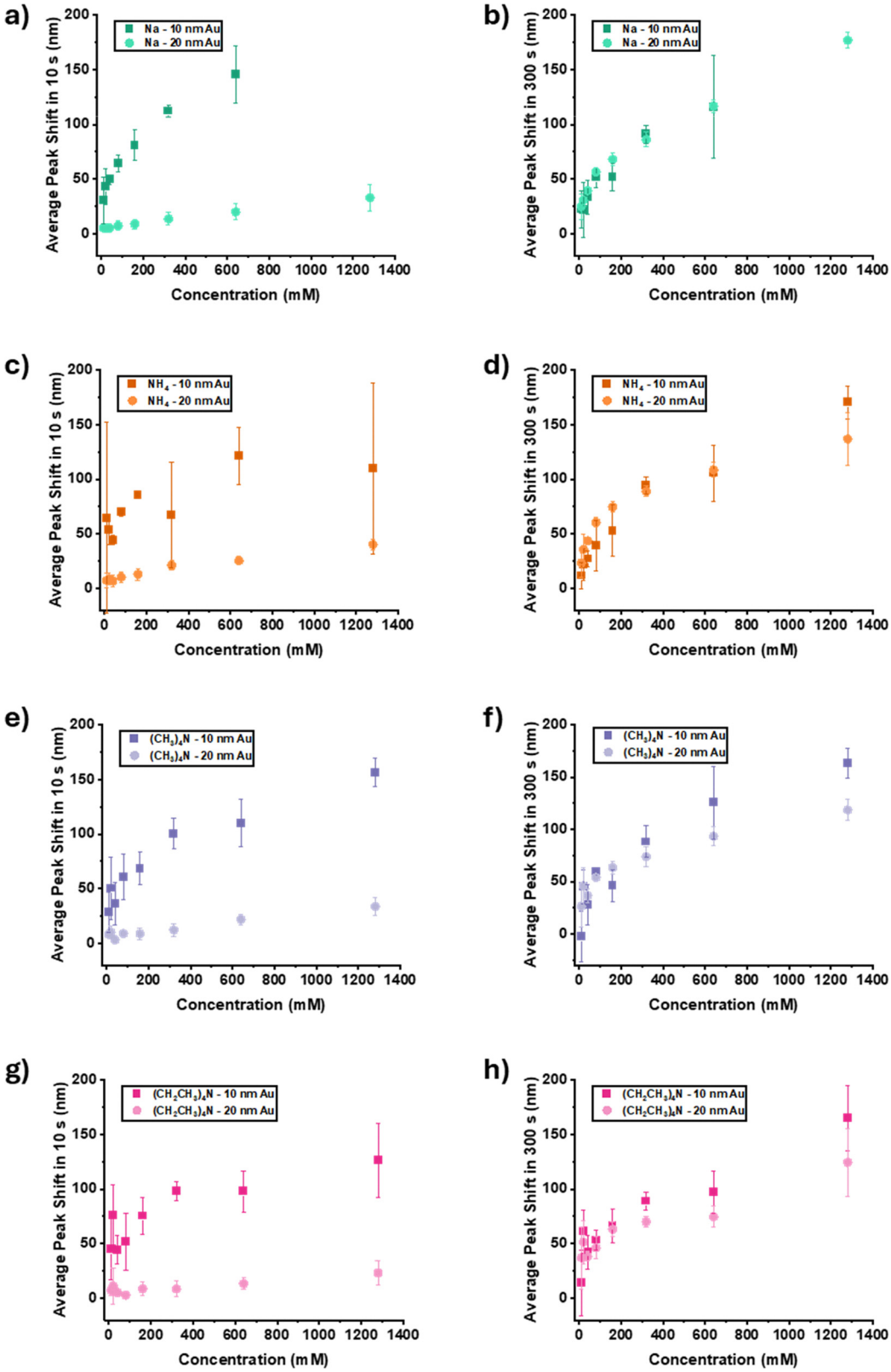

Fig. 9 Plots of peak shift over salt concentration of sodium chloride (a) and (b), ammonium chloride (c) and (d), tetramethylammonium chloride (e) and (f), and tetraethylammonium chloride (g) and (h) of both 10 nm Au and 20 nm Au overlayer etalons. The response after the first 10 s of salt exposure (a), (c), (e) and (g) and 300 s of exposure (b), (d), (f) and (h). 3 measurements at each concentration were taken per etalon and 3 different etalons of each overlayer type were measured. The average and standard deviation for an n = 9 are plotted.

 This journal is © The Royal Society of Chemistry 2026

Open Access Article. Published on 05 December 2025. Downloaded on 3/6/2026 5:47:09 PM.
This article is licensed under a Creative Commons Attribution 3.0 Unported Licence.

shifts of the etalons after the first 10 s of exposure to the salt solution (Fig. 9a, c, e and g) and the total peak shifts of the etalons after 5 min in the salt solution (Fig. 9b, d, f and h). The 20 nm Au etalons (continuous overlayer) have negligible response (except at 1280 mM) to all four cations initially. From this we can infer that the continuous overlayer of the etalon delays entry of various cations into the etalon cavity. Compared to this, the 10 nm Au etalons (discontinuous overlayer) exhibit noticeable, concentration-dependent peak shifts for all cations after initial exposure. We hypothesize, as with the previous experiments, that the discontinuous nature of the overlayer allows for immediate entry of the cations into the microgels within the etalon cavity. When the etalons are given time to equilibrate in the salt solutions the continuous overlayer etalons exhibit peak shifts nearly identical to that of the discontinuous overlayers, therefore we can say that the overlayer structure delays the etalon response to its environment but does not interfere with the overall final response. All the cations used in this study produced similar response patterns. It appears that for the polyatomic cations (ammonium, tetramethylammonium and tetramethylammonium) investigated, the etalons/microgels may be becoming saturated at lower concentrations than with the sodium ions, as their response curves have slightly reduced slopes. This will be explored in more depth in future experiments to determine if it can be exploited to tailor the sensitivity of the etalons. The knowledge that the rapid response of these etalons is not limited to specific cations is important for future studies on etalon-based point-of-need systems. We are working towards determining if this rapid response pattern is limited to salt response or if can be replicated with other analytes, such at DNA and other small molecules.

Conclusions

Here, we demonstrated that the composition of the metal overlayer influences the structure of the overlayer, at the microscopic scale, which is in turn integral to understanding how the etalons respond and how we can improve their function, *i.e.*, faster response time. The combination of metals (Cr and Au or Au) along with the overall thickness of the layer both impact the structure of the resulting film. This structure directly impacts how quickly the etalon can respond to a changing environment, whether it be hydration state or salt concentration. We have shown that this effect on response is robust to different cations and likely will hold true for other types of analytes in the future *i.e.*, nucleic acids, small molecules, and proteins. Moving forward, this work is being used by our researchers to develop point-of-need sensors to solve both health and environmental world problems.

Conflicts of interest

There are no conflicts to declare.

Data availability

The datasets generated during and/or analysed during the current study are not publicly available due to potential patent filings, but are available from the authors on reasonable request.

Acknowledgements

MJS acknowledges funding from the University of Alberta (the Department of Chemistry and the Faculty of Science), the Natural Sciences and Engineering Research Council of Canada (NSERC), the Canada Foundation for Innovation (CFI), the Alberta Advanced Education & Technology Small Equipment Grants Program (AET/SEGP), Grand Challenges Canada, and Future Energy Systems, NSERC CREATE (From Data to Decision), and Striving for Pandemic Preparedness—The Alberta Research Consortium.

References

1 T. Shu, H. Hunter, Z. Zhou, Y. Sun, X. Cheng, J. Ma, L. Su, X. Zhang and M. J. Serpe, Portable Point-of-Care Diagnostic Devices: An Updated Review, *Anal. Methods*, 2021, **13**(45), 5418–5435, DOI: 10.1039/D1AY01643A.

2 N. Jiang, N. D. Tansukawat, L. Gonzalez-Macia, H. C. Ates, C. Dincer, F. Güder, S. Tasoglu and A. K. Yetisen, Low-Cost Optical Assays for Point-of-Care Diagnosis in Resource-Limited Settings, *ACS Sens.*, 2021, **6**(6), 2108–2124, DOI: 10.1021/acssensors.1c00669.

3 C. Dincer, R. Bruch, E. Costa-Rama, M. T. Fernández-Abedul, A. Merkoçi, A. Manz, G. A. Urban and F. Güder, Disposable Sensors in Diagnostics, Food, and Environmental Monitoring, *Adv. Mater.*, 2019, **31**(30), 1806739, DOI: 10.1002/adma.201806739.

4 B. Ince and M. K. Sezgintürk, Lateral Flow Assays for Viruses Diagnosis: Up-to-Date Technology and Future Prospects, *TrAC, Trends Anal. Chem.*, 2022, **157**, 116725, DOI: 10.1016/j.trac.2022.116725.

5 L. Khelifa, Y. Hu, N. Jiang and A. K. Yetisen, Lateral Flow Assays for Hormone Detection, *Lab Chip*, 2022, **22**(13), 2451–2475, DOI: 10.1039/D1LC00960E.

6 H. Sohrabi, M. R. Majidi, P. Khaki, A. Jahanban-Esfahlan, M. de la Guardia and A. Mokhtarzadeh, State of the Art: Lateral Flow Assays toward the Point-of-Care Foodborne Pathogenic Bacteria Detection in Food Samples, *Compr. Rev. Food Sci. Food Saf.*, 2022, **21**(2), 1868–1912, DOI: 10.1111/1541-4337.12913.

7 J. Liu, M. Jalali, S. Mahshid and S. Wachsmann-Hogiu, Are Plasmonic Optical Biosensors Ready for Use in Point-of-Need Applications?, *Analyst*, 2020, **145**(2), 364–384, DOI: 10.1039/C9AN02149C.

8 J. Divya, S. Selvendran, A. S. Raja and A. Sivasubramanian, Surface Plasmon Based Plasmonic Sensors: A Review on Their Past, Present and Future, *Biosens. Bioelectron.: X*, 2022, **11**, 100175, DOI: 10.1016/j.biosx.2022.100175.

Open Access Article. Published on 05 December 2025. Downloaded on 3/6/2026 5:47:09 PM.
This article is licensed under a Creative Commons Attribution 3.0 Unported Licence.

9 J.-F. Masson, Portable and Field-Deployed Surface Plasmon Resonance and Plasmonic Sensors, *Analyst*, 2020, **145**(11), 3776–3800, DOI: 10.1039/D0AN00316F.
10 S. Qian, Y. Cui, Z. Cai and L. Li, Applications of Smartphone-Based Colorimetric Biosensors, *Biosens. Bioelectron.: X*, 2022, **11**, 100173, DOI: 10.1016/j.biosx.2022.100173.
11 W. K. Abdelbasset, S. V. Savina, D. Mavaluru, R. A. Shichiyakh, D. O. Bokov and Y. F. Mustafa, Smartphone Based Aptasensors as Intelligent Biodevice for Food Contamination Detection in Food and Soil Samples: Recent Advances, *Talanta*, 2023, **252**, 123769, DOI: 10.1016/j.talanta.2022.123769.
12 Y. Lin, Y. Li, H. Chang, S. Ye, Y. Ye, L. Yang, L. Liao, H. Dai, Z. Wei, Y. Deng, J. Zhang and C. Zheng, Rapid Testing of Δ9-Tetrahydrocannabinol and Its Metabolite On-Site Using a Label-Free Ratiometric Fluorescence Assay on a Smartphone, *Anal. Chem.*, 2023, **95**(18), 7363–7371, DOI: 10.1021/acs.analchem.3c00666.
13 R. S. Quimby, *Photonics and Lasers: An Introduction*, John Wiley & Sons, 2006.
14 Z. Zeng, J. Liang, R. Yu, J. Liu, M. Cao, S. Wang and Y. Xia, Programmable Color in a Free-Standing Photonic Microgel Film with Ultra-Fast Response, *ACS Appl. Mater. Interfaces*, 2021, **13**(21), 25563–25570, DOI: 10.1021/acsami.1c07099.
15 J. Qin, W. Wang and L. Cao, Photonic Hydrogel Sensing System for Wearable and Noninvasive Cortisol Monitoring, *ACS Appl. Polym. Mater.*, 2023, **5**(9), 7079–7089, DOI: 10.1021/acsapm.3c01119.
16 M. J. Serpe; C. D. Sorrell; M. C. D. Carter; I. N. Heppner; J. B. Smiley-Wiens and L. Hu, Color-Tunable Poly (N-Isopropylacrylamide) Microgel-Based Etalons: Fabrication, Characterization, and Applications, in *Hydrogel Micro and Nanoparticles*, John Wiley & Sons, Ltd, 2012, pp 317–336, DOI: 10.1002/9783527646425.ch13.
17 C. D. Sorrell and M. J. Serpe, Reflection Order Selectivity of Color-Tunable Poly(N-Isopropylacrylamide) Microgel Based Etalons, *Adv. Mater.*, 2011, **23**(35), 4088–4092, DOI: 10.1002/adma.201101717.
18 C. D. Sorrell, M. C. D. Carter and M. J. Serpe, A "Paint-On" Protocol for the Facile Assembly of Uniform Microgel Coatings for Color Tunable Etalon Fabrication, *ACS Appl. Mater. Interfaces*, 2011, **3**(4), 1140–1147, DOI: 10.1021/am1012722.
19 G. Brooker, Modern Classical Optics, in *Oxford Master Series in Physics*, Oxford University Press, Oxford, New York, 2003.
20 A. Halperin, M. Kröger and F. M. Winnik, Poly(N-Isopropylacrylamide) Phase Diagrams: Fifty Years of Research, *Angew. Chem., Int. Ed.*, 2015, **54**(51), 15342–15367, DOI: 10.1002/anie.201506663.
21 B. R. Saunders, On the Structure of Poly(N-Isopropylacrylamide) Microgel Particles, *Langmuir*, 2004, **20**(10), 3925–3932, DOI: 10.1021/la036390v.
22 Z. H. Farooqi, H. U. Khan, S. M. Shah and M. Siddiq, Stability of Poly(N-Isopropylacrylamide-Co-Acrylic Acid) Polymer Microgels under Various Conditions of Temperature, pH and Salt Concentration, *Arabian J. Chem.*, 2017, **10**(3), 329–335, DOI: 10.1016/j.arabjc.2013.07.031.
23 T. Widmann, L. P. Kreuzer, N. Hohn, L. Bießmann, K. Wang, S. Rinner, J.-F. Moulin, A. J. Schmid, Y. Hannappel, O. Wrede, M. Kühnhammer, T. Hellweg, R. von Klitzing and P. Müller-Buschbaum, Hydration and Solvent Exchange Induced Swelling and Deswelling of Homogeneous Poly(N-Isopropylacrylamide) Microgel Thin Films, *Langmuir*, 2019, **35**(49), 16341–16352, DOI: 10.1021/acs.langmuir.9b03104.
24 W. S. P. Carvalho, C. Lee, Y. Zhang, A. Czarnecki and M. J. Serpe, Probing the Response of Poly (N-Isopropylacrylamide) Microgels to Solutions of Various Salts Using Etalons, *J. Colloid Interface Sci.*, 2021, **585**, 195–204, DOI: 10.1016/j.jcis.2020.11.045.
25 T. López-León, J. L. Ortega-Vinuesa, D. Bastos-González and A. Elaissari, Thermally Sensitive Reversible Microgels Formed by Poly(N-Isopropylacrylamide) Charged Chains: A Hofmeister Effect Study, *J. Colloid Interface Sci.*, 2014, **426**, 300–307, DOI: 10.1016/j.jcis.2014.04.020.
26 T. López-León, A. Elaïssari, J. L. Ortega-Vinuesa and D. Bastos-González, Hofmeister Effects on Poly(NIPAM) Microgel Particles: Macroscopic Evidence of Ion Adsorption and Changes in Water Structure, *Chem. Phys. Chem.*, 2007, **8**(1), 148–156, DOI: 10.1002/cphc.200600521.
27 A. Moncho-Jordá and I. Adroher-Benítez, Ion Permeation inside Microgel Particles Induced by Specific Interactions: From Charge Inversion to Overcharging, *Soft Matter*, 2014, **10**(31), 5810–5823, DOI: 10.1039/C4SM00243A.
28 M. C. D. Carter, C. D. Sorrell and M. J. Serpe, Deswelling Kinetics of Color Tunable Poly(N-Isopropylacrylamide) Microgel-Based Etalons, *J. Phys. Chem. B*, 2011, **115**(49), 14359–14368, DOI: 10.1021/jp207138f.
29 W. Zhang, M. Wei, W. S. P. Carvalho and M. J. Serpe, Enzyme-Assisted Polymer Film Degradation-Enabled Biomolecule Sensing with Poly (N-Isopropylacrylamide)-Based Optical Devices, *Anal. Chim. Acta*, 2018, **999**, 139–143, DOI: 10.1016/j.aca.2017.11.012.
30 Y. Zhang, W. S. P. Carvalho, C. Fang and M. J. Serpe, Volatile Organic Compound Vapor Detection with Responsive Microgel-Based Etalons, *Sens. Actuators, B*, 2019, **290**, 520–526, DOI: 10.1016/j.snb.2019.03.147.
31 Y. Jiang, M. G. Colazo and M. J. Serpe, Poly(N-Isopropylacrylamide) Microgel-Based Sensor for Progesterone in Aqueous Samples, *Colloid Polym. Sci.*, 2016, **294**(11), 1733–1741, DOI: 10.1007/s00396-016-3926-3.
32 C. D. Sorrell and M. J. Serpe, Glucose Sensitive Poly (N-Isopropylacrylamide) Microgel Based Etalons, *Anal. Bioanal. Chem.*, 2012, **402**(7), 2385–2393, DOI: 10.1007/s00216-012-5736-x.
33 C. Jung, S.-J. Kim, J. Jang, J. H. Ko, D. Kim, B. Ko, Y. M. Song, S.-H. Hong and J. Rho, Disordered-Nanoparticle–Based Etalon for Ultrafast Humidity-Responsive Colorimetric Sensors and Anti-Counterfeiting Displays, *Sci. Adv.*, 2022, **8**(10), eabm8598, DOI: 10.1126/sciadv.abm8598.
34 T. Wang, S. Wang, X. Zhang, G. Song, Y. Yu, X. Chen, Y. Fu, J. Zhang and B. Yang, Responsive Etalon Based on PNIPAM@SiO2 Composite Spacer with Rapid Response Rate and Excellent Repeatability for Sensing Application,

 This journal is © The Royal Society of Chemistry 2026

Open Access Article. Published on 05 December 2025. Downloaded on 3/6/2026 5:47:09 PM.
This article is licensed under a Creative Commons Attribution 3.0 Unported Licence.

Nanotechnology, 2015, **26**(28), 285501, DOI: 10.1088/0957-4484/26/28/285501.

35 Y. Dong, E. M. Akinoglu, H. Zhang, F. Maasoumi, J. Zhou and P. Mulvaney, An Optically Responsive Soft Etalon Based on Ultrathin Cellulose Hydrogels, *Adv. Funct. Mater.*, 2019, **29**(40), 1904290, DOI: 10.1002/adfm.201904290.

36 T. J. Palinski, T. J. Palinski, A. Tadimety, I. Trase, B. E. Vyhnalek, G. W. Hunter, E. Garmire and J. X. J. Zhang, Vibrant Reflective Sensors with Percolation Film Fabry-PéRot Nanocavities, *Opt. Express*, 2021, **29**(16), 25000–25010, DOI: 10.1364/OE.432097.

37 A. Escher, H. Megahd, C. Tavella, D. Comoretto and P. Lova, Colorimetric Polymer Sensors for Smart Packaging, *Macromol. Chem. Phys.*, 2023, **224**(14), 2300022, DOI: 10.1002/macp.202300022.

38 Z. Meng, M. Smith and L. Lyon, Temperature-Programmed Synthesis of Micron-Sized Multi-Responsive Microgels, *Colloid Polym. Sci.*, 2009, **287**, 277–285, DOI: 10.1007/s00396-008-1986-8.

39 A. Fu and M. J. Serpe, Electrochromic Microgel-Based Etalon Devices, *ACS Appl. Polym. Mater.*, 2022, **4**(12), 9186–9193, DOI: 10.1021/acsapm.2c01469.

40 J. B. Smiley-Wiens and M. J. Serpe, Solvent Exchange Kinetics in Poly(N-Isopropylacrylamide) Microgel-Based Etalons, *Colloid Polym. Sci.*, 2013, **291**(4), 971–979, DOI: 10.1007/s00396-012-2818-4.

41 M. Schneider, H. Möhwald and S. Akari, Quantitative Measurement of Chromium's Ability to Promote Adhesion, *J. Adhes.*, 2003, **79**(6), 597–607, DOI: 10.1080/00218460309539.

42 R. L. W. Smithson, D. J. McClure and D. Fennell Evans, Effects of Polymer Substrate Surface Energy on Nucleation and Growth of Evaporated Gold Films, *Thin Solid Films*, 1997, **307**(1), 110–112, DOI: 10.1016/S0040-6090(97)00310-6.

43 O. Graudejus, P. Görrn and S. Wagner, Controlling the Morphology of Gold Films on Poly(Dimethylsiloxane), *ACS Appl. Mater. Interfaces*, 2010, **2**(7), 1927–1933, DOI: 10.1021/am1002537.

44 F. C. Löhrer, V. Körstgens, G. Semino, M. Schwartzkopf, A. Hinz, O. Polonskyi, T. Strunskus, F. Faupel, S. V. Roth and P. Müller-Buschbaum, Following in Situ the Deposition of Gold Electrodes on Low Band Gap Polymer Films, *ACS Appl. Mater. Interfaces*, 2020, **12**(1), 1132–1141, DOI: 10.1021/acsami.9b17590.

45 P. Šmilauer, Thin Metal Films and Percolation Theory, *Contemp. Phys.*, 1991, **32**(2), 89–102, DOI: 10.1080/00107519108213805.

46 S. Norrman, T. Andersson, C. G. Granqvist and O. Hunderi, Optical Properties of Discontinuous Gold Films, *Phys. Rev. B: Condens. Matter Mater. Phys.*, 1978, **18**(2), 674–695, DOI: 10.1103/PhysRevB.18.674.

47 G. D. T. Spiller and M. Hanbucken, Nucleation and Growth of Thin Films.

48 Atomistic Processes in the Early Stages of Thin-Film Growth, DOI: 10.1126/science.276.5311.377.

49 D. M. Mattox, Chapter 10 – Atomistic Film Growth and Some Growth-Related Film Properties, in *Handbook of Physical Vapor Deposition (PVD) Processing*, ed. Mattox, D. M., William Andrew Publishing, Boston, 2nd edn, 2010; pp 333–398, DOI: 10.1016/B978-0-8155-2037-5.00010-1.